Monthly Notices
of the
ROYAL ASTRONOMICAL SOCIETY

MNRAS **506,** 5389–5397 (2021) https://doi.org/10.1093/mnras/stab1965

uGMRT detection of cluster radio emission in low-mass *Planck* Sunyaev–Zel'dovich clusters

Surajit Paul [1]★ Prateek Gupta,[1] Sameer Salunkhe [1] Shubham Bhagat,[1] Satish Sonkamble [2] Manish Hiray,[1] Pratik Dabhade[3,4,5] and Somak Raychaudhury [4,6]

[1]*Department of Physics, Savitribai Phule Pune University, Pune 411007, India*
[2]*INAF-Padova Astronomical Observatory, Vicolo dell'Osservatorio 5, I-35122 Padova, Italy*
[3]*Leiden Observatory, Leiden University, Niels Bohrweg 2, 2333 CA, Leiden, The Netherlands*
[4]*Inter-University Centre for Astronomy and Astrophysics, Pune 411007, India*
[5]*Observatoire de Paris, LERMA, Collège de France, CNRS, PSL University, Sorbonne University, 75014, Paris, France*
[6]*School of Physics and Astronomy, University of Birmingham, Birmingham B15 2TT, UK*

Accepted 2021 July 6. Received 2021 June 29; in original form 2021 February 23

ABSTRACT

Low-mass ($M_{500} < 5 \times 10^{14}$ M$_\odot$) galaxy clusters have been largely unexplored in radio observations, because of the inadequate sensitivity of existing telescopes. However, the upgraded Giant Metrewave Radio Telescope (uGMRT) and the Low Frequency ARray (LoFAR), with unprecedented sensitivity at low frequencies, have paved the way to study less massive clusters more closely than before. We have started the first large-scale programme to systematically search for diffuse radio emission from low-mass galaxy clusters, chosen from the *Planck* Sunyaev–Zel'dovich cluster catalogue. We report here the detection of diffuse radio emission from four of the 12 objects in our sample, shortlisted from the inspection of the LoFAR Two-Meter Sky Survey data release 1 (LoTSS-I), followed up by uGMRT Band 3 deep observations. The clusters PSZ2 G089 (Abell 1904) and PSZ2 G111 (Abell 1697) are detected with relic-like emission, while PSZ2 G106 is found to have an intermediate radio halo and PSZ2 G080 (Abell 2018) seems to be a halo-relic system. PSZ2 G089 and PSZ2 G080 are among the lowest-mass clusters discovered with a radio-relic and a halo-relic system, respectively. A high (∼30 per cent) detection rate, with powerful radio emission ($P_{1.4\,\mathrm{GHz}} \sim 10^{23}$ W Hz^{-1}) found in most of these objects, opens up prospects of studying radio emission in galaxy clusters over a wider mass range, to much lower-mass systems.

Key words: galaxies: clusters: general – large-scale structure of Universe – radio continuum: general – X-rays: galaxies: clusters.

1 INTRODUCTION

Observations of diffuse radio emission due to synchrotron processes reveal the dynamical state and the non-thermal energy evolution in galaxy clusters. Though massive clusters ($>5 \times 10^{14}$ M$_\odot$) have been detected in abundance at radio frequencies over the last few decades (e.g. van Weeren et al. 2019), the less massive clusters ($<5 \times 10^{14}$ M$_\odot$) have remained largely unexplored. This is mainly because of limitations in sensitivity at the usual radio frequencies. Further, the dearth of theoretical estimates for favourable detections in low-mass systems, with the currently available instruments, has so far discouraged systematic studies. For instance, while the theoretical prediction of Cassano et al. (2010) shows a low probability for halo detection in low-mass clusters with the Low Frequency ARray (LoFAR), the recent analysis of Very Large Array (VLA) and Giant Metrewave Radio Telescope (GMRT) data of 75 high-mass clusters with radio haloes by Cuciti et al. (2021) shows a large scatter in the radio power–mass correlation, leading to broader confidence levels at the lower-mass end, indicating the prospect of a better detectable fraction of radio haloes from them. It can be noted that, before the upgraded GMRT (uGMRT) and LoFAR, only a handful of low-mass clusters had been detected with cluster radio emission (Bernardi et al. 2016; de Gasperin et al. 2017; Kale et al. 2017; Dwarakanath et al. 2018; Botteon et al. 2019; Knowles et al. 2019). However, in the absence of their detection, the understanding of the hierarchical formation of clusters, especially in the non-thermal regime, would remain incomplete.

Radio emission linked to the tenuous plasma of the intracluster medium (ICM) is diffuse in nature, with very low surface brightness (∼μJy arcsec^{-2}) and a steep spectrum ($\alpha < -1$, with $S_\nu \propto \nu^\alpha$). Such detections are usually hundreds of kpc to Mpc in extent, and are mostly found in merging systems. Depending on their location in the cluster and the possible process of origin, they are divided into two major classes (Feretti et al. 2012). Such diffuse and feebly (<5 per cent) polarized centrally located, emission, possibly resulting from the turbulence in the ICM, is generally termed a 'radio halo'. In contrast, comparatively strongly polarized (∼30 per cent) 'radio relics' usually originate from cluster merger shocks, and are mostly located at the cluster outskirts. Objects of a third kind, with central diffuse radio emission, but smaller in extent (100–500 kpc), are known as radio 'mini-haloes'. These are usually found around the brightest cluster galaxy (BCG) in relaxed clusters with cool cores, and their emission is thought to be of hadronic origin, that is, from the

★ E-mail: surajit@physics.unipune.ac.in

secondary electrons produced from the central active galactic nucleus (AGN; e.g. Ferrari et al. 2008; Giacintucci et al. 2019; Ignesti et al. 2020).

Diffuse radio sources in clusters have so far been detected mostly in massive systems (van Weeren et al. 2019). However, in various studies of low-mass clusters, evidence of mergers and non-gravitational processes (e.g. Lovisari, Reiprich & Schellenberger 2015) is frequently observed, and AGN feedback processes are known to significantly affect such systems (e.g. Gaspari et al. 2011). Recent simulations of the evolution of turbulence and cosmic rays in low-mass systems show significant deviations from scaling relations found in richer clusters, having flatter slopes and higher fluctuations (e.g. Paul et al. 2017; John et al. 2019), indicating that more of them should be detectable because of their non-thermal properties. Furthermore, as low-mass systems are cooler than massive systems, the Mach number of the shocks in the ICM, which depends on the ICM temperature, would be noticeably higher in these sources (Sarazin 2002). This would mean more and more low-mass clusters would become observable with diffuse radio emission as the sensitivity of radio telescopes improves, as is already happening (see, e.g., the review by van Weeren et al. 2019). The unprecedented sensitivity of LoFAR ($\sim$100 μJy at 144 MHz) has revolutionized the study of diffuse emission in low-mass systems (Hoang et al. 2019; Knowles et al. 2019; Botteon et al. 2019; Paul et al. 2020), particularly the emission linked with the ICM in groups (Nikiel-Wroczyński et al. 2019).

Our study begins with a serendipitous discovery of a radio relic and trailing emission in a low-mass cluster, Abell 1697 (Paul et al. 2020), from the LoFAR Two-Meter Sky Survey data release 1 (LoTSS-I). Thereafter, we started a programme to systematically search for low-mass ($M < 5 \times 10^{14}$ $M_\odot$) systems listed in the *Planck* Sunyaev–Zel'dovich (SZ) galaxy cluster catalogue (Planck Collaboration 2016, hereafter Planck-16), in the region overlapping that of LoTSS-I. Mosaic images from LoTSS-I are reported to suffer from different types of artefacts, such as low-level positive or negative haloes (Shimwell et al. 2019), making it difficult to precisely characterize faint diffuse sources, particularly because the raw data are not publicly available for reprocessing. This led us to obtain fresh deep observations at a complementary frequency, with uGMRT at Band 3, to confirm the *Planck* SZ systems for which we found evidence of diffuse emission in LoTSS-I. Further, to understand the nature of the detected radio emission, we went on to study the optical and X-ray properties of these systems using publicly available archival data.

In this paper, we report on the detection of cluster radio emission from four low-mass galaxy clusters. Following the details of data selection and analysis presented in Section 2, we discuss the LoTSS-I radio detection and the follow-up uGMRT observations, along with the multiwavelength properties of these systems, in Section 3. Our conclusions are outlined in Section 4. A ΛCDM cosmology is assumed with parameters $H_0 = 70$ km s^{-1} Mpc^{-1}, $\Omega_M = 0.3$ and $\Omega_\Lambda = 0.7$ throughout the paper.

2 DATA SELECTION AND ANALYSIS

We have produced a list of low-mass clusters ($\lesssim 5 \times 10^{14}$ $M_\odot$), from a total of 1653 objects published in the latest *Planck* SZ galaxy cluster catalogue (Planck-16). Because our goal is to first check the LoTSS-I (Shimwell et al. 2019) for evidence of diffuse emission, before following-up with uGMRT, we select only those clusters located in the area of the sky between RA 161.°25 and 232.°5 and Dec. +45° and +57°. This resulted in 14 objects (see Table 1), for which the LoTSS images are publicly available. We then visually inspected each of them in the LoTSS-I maps and found that two of these fall outside the edges of the provided mosaics. Finally, among the remaining 12 objects, four clusters – PSZ2 G080.16+57.65 (PSZ2 G080), PSZ2 G089.52+62.34 (PSZ2 G089), PSZ2 G106.61+66.71 (PSZ2 G106) and PSZ2 G111.75+70.37 (PSZ2 G111) – are found to have indications of diffuse radio emission, whereas the remaining eight objects are devoid of any diffuse emission at the local rms noise level, as given in Table 1. Of these, images of PSZ2 G096.14+56.24 and PSZ2 G123.66+67.25 are significantly affected by the point spread function side lobes of the central bright sources (flux >1 Jy). Independently, all four of these appear in the LoTSS sample of cluster radio sources (van Weeren et al. 2020). We then obtained the uGMRT (Gupta et al. 2017) Band 3 (300–500 MHz) data (proposal code: ddtC 157) with $\sim$2 h on-source time on each of these objects.

Table 1. Selected low-mass clusters from the *Planck* SZ cluster list and LoTSS-I maps. Note that an asterisk indicates observed with uGMRT and NDE denotes no diffuse emission. Structures are indicated as relic (R), halo (H), intermediate halo (iH) and trailing emission (T).

Object	M_{500}^{SZ} $M_\odot$ (10^{14})	z	LoTSS indication	rms noise (μJy B^{-1})[a]
∗ PSZ2 G080.16+57.65	2.51	0.08780	H&R	240
PSZ2 G088.98+55.07	4.92	0.70235	NDE	180
∗ PSZ2 G089.52+62.34	1.83	0.07008	cR	200
PSZ2 G095.22+67.41	1.50	0.06250	NDE	100
PSZ2 G096.14+56.24	2.77	0.13977	NDE	160
PSZ2 G098.44+56.59	2.83	0.13184	NDE	160
PSZ2 G099.48+55.60	2.81	0.10510	Outside	–
∗ PSZ2 G106.61+66.71	4.67	0.33140	iH?	300
∗ PSZ2 G111.75+70.37	4.34	0.18300	R&T	420
PSZ2 G118.34+68.79	3.77	0.25488	NDE	150
PSZ2 G123.66+67.25	4.38	0.28380	NDE	130
PSZ2 G136.92+59.46	1.81	0.06500	Outside	–
PSZ2 G144.33+62.85	2.66	0.13200	NDE	120
PSZ2 G145.65+59.30	4.73	0.34748	NDE	110

[a]The beam size (B) is 20×20 arcsec^2 for all the objects except for PSZ2 G111, for which it is 25×25 arcsec^2.

Table 2. The uGMRT imaging parameters, with those for the point-source subtracted images given within parentheses.

Object	Robust	Taper (arcsec)	Beam (arcsec)	rms (μJy B^{-1})
PSZ2 G080	0.5 (1.0)	10.0 (8.0)	34×17 (65×24)	55 (120)
PSZ2 G089	0.5	5.0	15×12	50
PSZ2 G106	0.5 (1.0)	0.0 (10.0)	11×7 (35×17)	45 (120)
PSZ2 G111	0.0/1.0	10.0/10.0	13×10/21×16	65/100

Data reduction and imaging were primarily performed using the SPAM pipeline (for details, see Intema et al. 2017). This is a powerful data analysis and imaging pipeline that takes care of direction-dependent variations (i.e. due to the antenna beam pattern and the ionosphere) in visibility, amplitude and phase, across the field of view. Using SPAM, wide-band uGMRT data were first split into six narrower bands, and each of these bands was initially calibrated for flux and bandpass using the source 3C 286. The final SPAM-calibrated data for each narrow band, after imaging, were combined to produce wide-band images using the WSCLEAN package (Offringa et al. 2014), with the specific parameters as mentioned in Table 2. To

Table 3. Radio (400 MHz uGMRT and 144 MHz LoTSS maps, for the same area as uGMRT observations) and X-ray (0.5–8 keV *XMM* and 0.5–3 keV *Chandra*) properties. Here, H, R and T represent halo, relic and trailing emission, respectively.

Object	Abell name	$S_{400}(3\sigma)$ (mJy)	LoTSS-I flux[a] (mJy)	S_{144}[b] (mJy)	Size (uGMRT, kpc)	Model halo flux (mJy)	Model halo diameter (kpc)	L_X (10^{44} erg s^{-1})
PSZ2 G080 (H)	Abell 2018	19.3 ± 2.0	72.1 ± 17.1	92 ± 32	540×490	18.0 ± 0.5	493 ± 21	$0.81^{+0.01}_{-0.01}$
(R)		13.3 ± 1.4	–	55.8 ± 11.6	1000	–	–	–
PSZ2 G089 (cR)	Abell 1904	6.6 ± 0.7	19.9 ± 3.1	74.6 ± 15.0	205×45	–	–	$2.54^{+0.03}_{-0.02}$
PSZ2 G106 (iH)	–	8.6 ± 1.0	23.9 ± 4.9	20 ± 4	550×530	6.6 ± 0.2	507 ± 17	$3.97^{+0.40}_{-0.10}$
PSZ2 G111 (R)	Abell 1697	49.7 ± 5.0	130.2 ± 26.1	106.7 ± 21.4	750×350	–	–	$5.26^{+0.30}_{-0.40}$
(T)		15.3 ± 1.6	41.7 ± 8.3	–	450×350	–	–	–

[a] Flux density for the same area as uGMRT 3σ area. [b] As reported in van Weeren et al. (2020).

make point-source subtracted low-resolution images, high-resolution point-source only images were first produced using an appropriate 'uvcut' in WSCLEAN and then the point sources were subtracted from the UV data, using the FT and UVSUB tasks in CASA.

The radio flux densities (S) were measured within 3σ contours of each map (where σ is the local rms noise), and flux density errors were estimated (σ_S) using the relation $\sigma_S = \sqrt{(f \times S)^2 + N\sigma^2 + \sigma_{\rm sub}^2}$, where N is the number of beams within 3σ contours and $\sigma_{\rm sub}$ is the uncertainty due to compact source subtraction (applied to the point-source subtracted maps). We assumed an usual $f = 10$ per cent for uGMRT and $f = 20$ per cent for LoTSS-I (as mentioned in Shimwell et al. 2019) of S to be the error due to calibration uncertainties. In addition to the usual method of flux density measurements within 3σ isophotes in radio images, we employed a more generic method to compute the radio flux density of halo-type diffuse radio sources in galaxy clusters, by fitting azimuthally averaged brightness profiles with an exponential function (Murgia et al. 2009). The fitted exponential profile is of the form $I(r) = I_0 \exp\ -\ (r/r_{\rm e})$, where $r_{\rm e}$ is the characteristic e-folding radius and I_0 is the peak surface brightness of the radio halo. Profiles were fit using a least-squares fitting algorithm. For statistical purposes, in each radio image, the surface brightness was sampled several times with different linear radial step sizes. Corresponding to the fitting parameters, I_0 and $r_{\rm e}$, for each surface brightness sampling, the flux densities were measured by integrating the fitted brightness profile up to three times the e-folding radius (i.e. $3r_{\rm e}$), following Murgia et al. (2009). Accordingly, the statistical mean and standard deviation of fitted flux densities for each halo are reported in Table 3. All images used in this paper were manipulated and analysed using the CASA package (McMullin et al. 2007).

For multiwavelength follow-up, we obtained (optical) data from the Panoramic Survey Telescope and Rapid Response System (Pan-STARRS1) for all the objects and, in X-rays, *XMM–Newton* data of ∼35 ks (ObsID:0821040401), ∼15 ks (ObsID:0821040301) and ∼44 ks (ObsID:0827020801) for PSZ2 G080, PSZ2 G089 and PSZ2 G111, respectively, and the *Chandra* observations for PSZ2 G106 (15 ks, ObsID:21708). The *Chandra* data were reduced using CIAO v4.11 and CALDB 4.8.4, following the standard data reduction threads, and using re-projected blank-sky background files. The *XMM–Newton* data were analysed using SAS v18 and the latest calibration files. We used the IMAGES tool to clean high background flares, to apply exposure corrections, to perform spatial smoothing, and to create and combine PN and MOS images. Spectral extraction and fitting were performed in XSPEC v12.10.1 with the fitted `tbabs×apec` model in the 0.5–8.0 keV energy band to compute X-ray luminosities within r_{500} of each source. The X-ray surface brightness profiles were extracted and fitted using PROFFIT v1.5 (Eckert, Molendi & Paltani 2011).

3 DETECTION FROM LOTSS-I AND UGMRT BAND 3

The measured parameters of these newly detected objects with cluster radio emission from uGMRT and LoTSS-I are outlined in Table 3. The details of individual objects are individually presented below.

3.1 A candidate radio relic in cluster PSZ2 G089.52+62.34

This is a low-redshift ($z = 0.07008$) cluster with SZ mass $M_{500}^{\rm SZ} = 1.83^{+0.19}_{-0.20} \times 10^{14}$ M$_\odot$ (Planck-16). The rich galaxy cluster Abell 1904 is located well within this source, ∼4 arcmin away from the centre of PSZ2 G089. The reported one-dimensional velocity dispersion of the Abell cluster is 803 km s^{-1} (Struble & Rood 1999), which is a high value given its mass, and might be indicative of an ongoing merger. This is consistent with the elongated mass distribution along the SW to NE direction (Flin & Krywult 2006), the evidence of substructures found in our *XMM* maps and the high X-ray luminosity ($L_{\rm X} = 2.54^{+0.03}_{-0.02} \times 10^{44}$ erg s^{-1}) of the source.

A peripheral diffuse radio structure was noticed towards the NE of this cluster in the low-resolution image from LoTSS-I (local $\sigma_{144} = 200$ μJy beam^{-1}; see Fig. 1a). In our uGMRT Band 3 image, we also detect this peripheral radio emission, and it is shown as black contours within the blue-dashed polygonal area in Fig. 1(a). The largest linear size (LLS) and width of this elongated diffuse emission, as measured in the uGMRT maps, are 205 kpc and 45 kpc, respectively. Its flux density is $S_{400} = 6.6 \pm 0.7$ mJy at uGMRT Band 3 and, for the same region, the LoTSS-I flux density is estimated to be $S_{144} \sim 19.9 \pm 3.1$ mJy. van Weeren et al. (2020) have reported a larger relic, as well as a second part of the relic, in their improved LoTSS-II images. This could not be detected in our uGMRT maps (at a higher frequency) at the reported rms noise level of 50 μJy beam^{-1}. Such morphological dissimilarity between images at different frequencies is common for steep-spectrum radio sources.

In Fig. 1(a), uGMRT contours are overlaid on a Pan-STARRS1 optical image, where no optical counterpart of this diffuse radio emission is seen. The *XMM* X-ray contours show two prominent substructures, marked as 'A' and 'B' in Fig. 1(b), possibly in the process of merger along the SW to NE direction. As is usual for radio relics, the convex and elongated radio structure at the outskirts of this cluster coincides with the outer X-ray contours, placed well ahead of the merging clumps, perpendicular to the merging axis (see Fig. 1b). This structure is found about 4 arcmin away from the bigger X-ray substructure (A). Though clear evidence of a thermal shock is absent in the low-exposure (15-ks) *XMM* data, interestingly, a sudden dip in the X-ray surface brightness profile, for the sector $100^\circ - 170^\circ$ shown in Fig. 1(d), with a residual of more than 2σ from the β-model fit (see Fig. 1c), certainly indicates the presence of an apparent shock front at a similar distance (∼4 arcmin) as the radio diffuse emission.

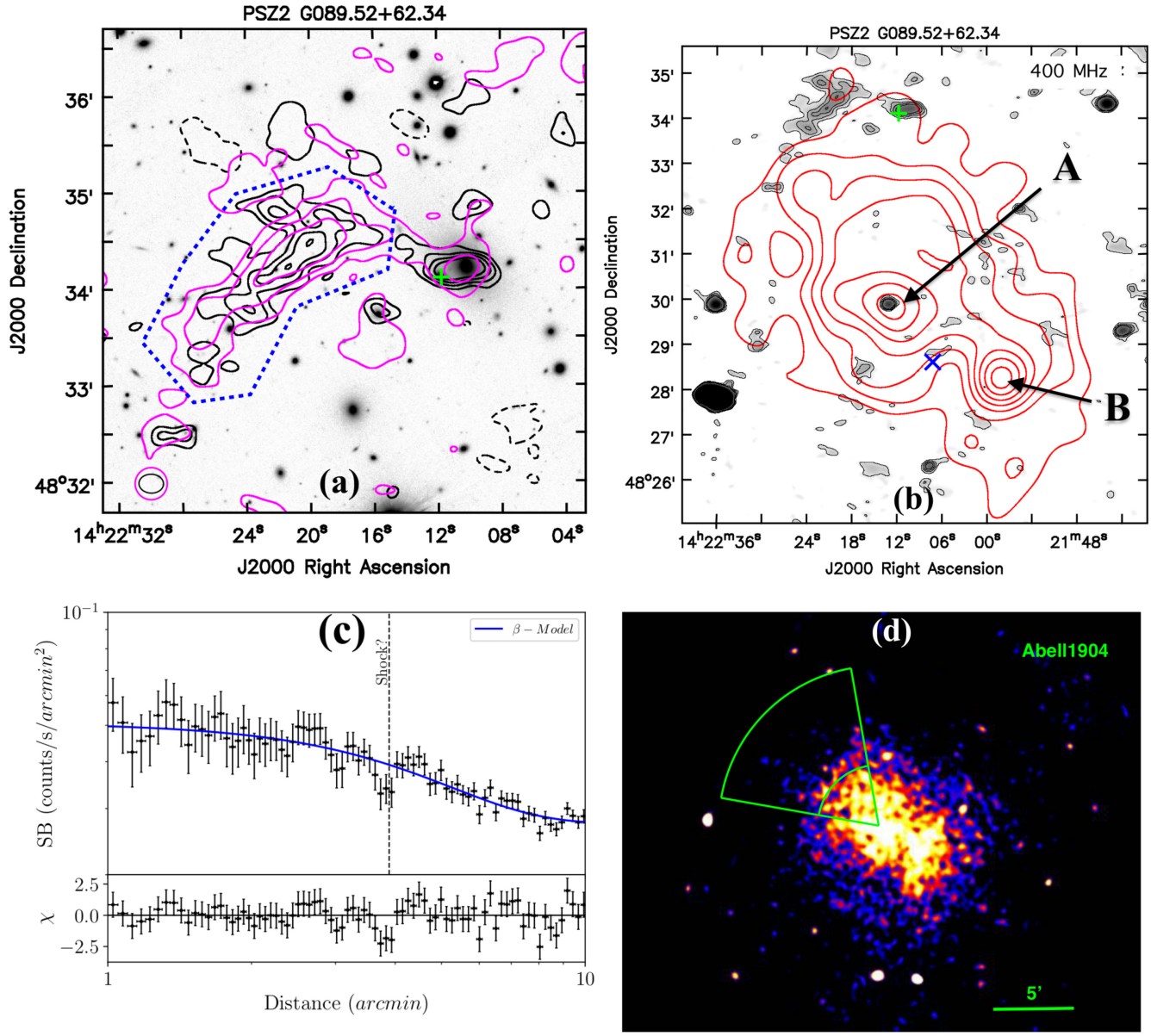

Figure 1. (a) Contours of uGMRT (black, at $-3, 3, 5, 7, 9, 18 \times \sigma_{400}$) and LoTSS-I (magenta, at $-3, 3, 6, 9, 18 \times \sigma_{144}$) of PSZ2 G089.52+62.34 are plotted over the Pan-STARRSI *i*-band image. (b) X-ray contours plotted on the uGMRT (greyscale) image and contour maps. The *Planck* SZ centre is marked as a blue '×' and the Abell cluster centre as a green '+' for all the images in this paper. The physical scale for the images is 1.34 kpc arcsec^{-1} (c) The X-ray surface brightness profile fitted with the β-model and its residues, for the sector 100°–170°, as shown in (d).

Because van Weeren et al. (2020) have provided the combined flux density for two parts of the relic and we could detect only one part of it in our uGMRT maps, it was not possible to compute a meaningful spectral index. We have, however, made a rough estimate of an average spectral index between the uGMRT detection and its co-located LoTSS-I counterpart, found to be $\alpha_{144}^{400} \sim -1.08$, suggesting a case of relic emission. In the absence of stronger evidence, we classify it as a candidate relic.

3.2 A radio relic and trailing emission in PSZ2 G111.75+70.37

PSZ2 G111.75+70.37, identified with the poor cluster Abell 1697, is a moderately distant cluster at a spectroscopic redshift of $z = 0.1813$. The estimated mass for the cluster in the Planck-16 catalogue is $M_{500}^{SZ} = 4.34^{+0.32}_{-0.33} \times 10^{14}$ M$_\odot$ and its estimated *XMM* X-ray luminosity is $L_X = 5.26^{+0.30}_{-0.40} \times 10^{44}$ erg s^{-1}. This cluster is reported to host a radio relic and an ultra-steep spectrum trailing emission, as tentatively computed from LoTSS-I and NVSS maps (Paul et al. 2020).

In this case, we detect both the radio structures in our uGMRT band 3 low-resolution map (see Fig. 2a; rms noise $\sigma_{400} = 100$ μJy beam^{-1}), similar to those seen in LoTSS-I ($\sigma_{144} = 420$ μJy beam^{-1}). However, no clear evidence of radio halo emission, as found by van Weeren et al. (2020), could be seen in our maps.

The relic is 750 kpc long and 350 kpc in width (marked as 'R' in Fig. 2a), having a uGMRT flux $S_{400}(R) = 49.7 \pm 5.0$ mJy. The distance from the *Planck* cluster centre to the peak relic emission is about 850 kpc. The trailing emission (marked as 'T' and enclosed

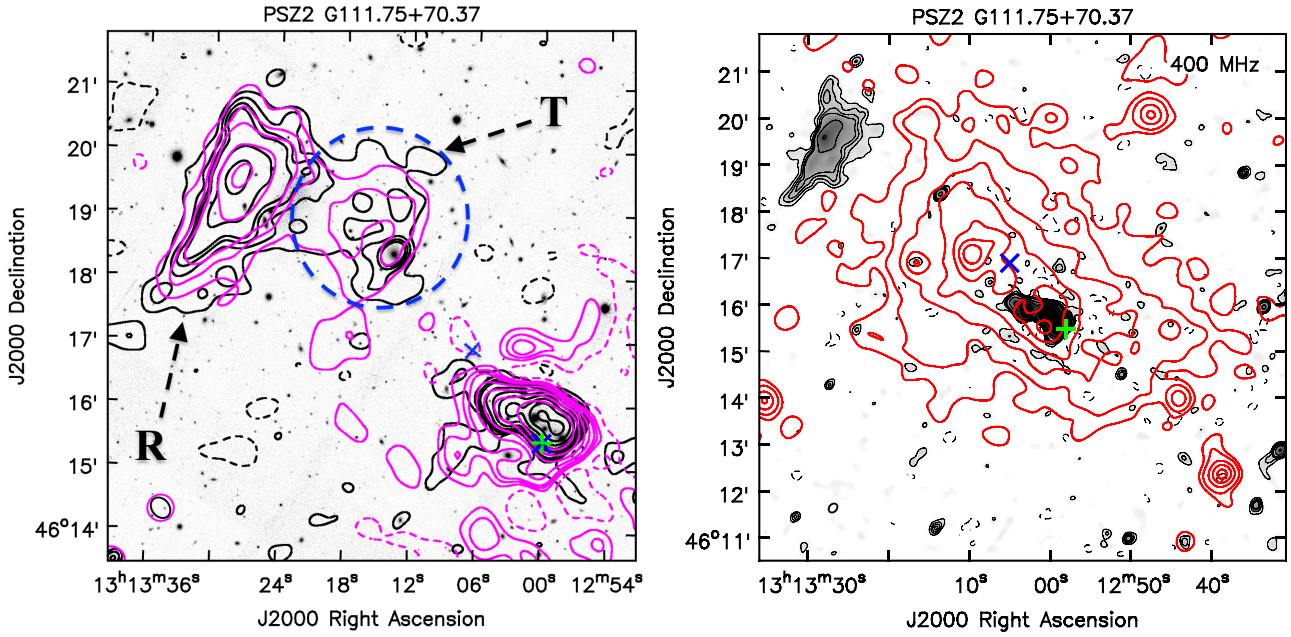

Figure 2. (a) uGMRT and LoTSS-I contours are plotted on the PanSTARSS-I *i*-band image of source PSZ2 G111.75+70.37. Contours (levels same as in Fig. 1) of uGMRT (black), LoTSS-I (magenta) with rms noise of 100 and 420 μJy beam^{-1}, respectively. (b) *XMM* contours (red) are plotted over the uGMRT high-resolution greyscale image and contour maps (at -3, 3, 6, 9, 18, 36 $\times$ σ, where σ = 65 μJy beam^{-1}). The physical scale for the images is 3.05 kpc arcsec^{-1}.

within the dashed ellipse) is large, about 450 $\times$ 350 kpc in projected extent, but is very faint, $S_{400}(T) = 15.3 \pm 1.6$ mJy.

The LoTSS-I flux for the two detected structures and the same region as uGMRT are $S_{144}(R) \sim 130.2 \pm 26.1$ mJy and $S_{144}(T) \sim 41.7 \pm 8.3$ mJy. Accurate spectral index estimation with these values would not be possible because the LoTSS-I map that is available to us for this object is contaminated with significant artefacts, as mentioned in van Weeren et al. (2020).

Fortunately, the NVSS map for this cluster contains a detection of a major part of the relic. Combining the images at 1.4 GHz (NVSS) and the matched *uv*-coverage map at 400 MHz (uGMRT), we produced a spectral index map, as shown in Fig. 3. The average spectral index of the proposed relic part (i.e. 'R', common area with 3σ detection of NVSS) is about $\alpha_{\rm int}^{1420}_{400} = -1.40 \pm 0.01$. The spectral index at the relic front is $\alpha_{\rm inj} = -0.93 \pm 0.01$, which gradually steepens to $\alpha_{\rm tail} = -1.87 \pm 0.01$ towards the inside edge of the relic. Therefore, it reasonably follows the predictions of the commonly used continuous injection spectrum model for radio relics (i.e. $\alpha_{\rm inj}^{1420}_{400} = -0.93 \sim \alpha_{\rm int}^{1420}_{400} + 0.5$).

Our *XMM–Newton* contours in Fig. 2(b) clearly show substructures merging along the SW to NE direction, and the relic is found ahead of this at the cluster outskirts, perpendicular to the merging axis. This is suggestive of a typical binary merger of clusters producing peripheral radio relics. All the possible scenarios for the origin of radio emission in this cluster have been discussed in detail in Paul et al. (2020).

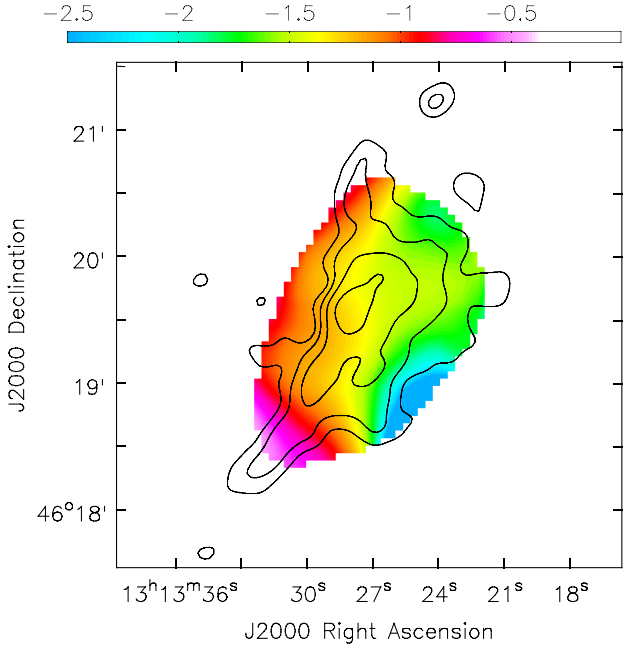

Figure 3. Spectral index map of the relic found in the cluster PSZ2 G111.75+70.37, prepared using the uGMRT (400 MHz) and NVSS (1.4 GHz) images.

3.3 A radio halo–relic system in cluster PSZ2 G080.16+57.65

PSZ2 G080.16+57.65 (or PSZ2 G080 for short), also identified with the cluster Abell 2018, is another low-redshift ($z = 0.0878$) poor cluster in our sample, having mass $M_{500}^{\rm SZ} = 2.51^{+0.20}_{-0.21} \times 10^{14}$ M$_\odot$ (Planck-16), and a moderate X-ray luminosity $L_{\rm X} = 8.14^{+0.04}_{-0.03} \times 10^{43}$ erg s^{-1}. A cluster called GMBCG J225.28318+47.27663 (Hao et al. 2010), shown as a magenta cross in Fig. 4(b), is within 2 arcmin of PSZ2 G080, with a comparable redshift $z = 0.0882$ and mass $M = 2.86 \pm 0.26 \times 10^{14}$ M$_\odot$, indicating that they are the same object.

We found a large, 1-Mpc peripheral bow-like structure and an indication of diffuse radio emission in the central region of this cluster in our uGMRT high-resolution map (see Fig. 4a). The peripheral structure in this cluster is very faint with a flux $S_{400} = 13.3 \pm 1.4$ mJy,

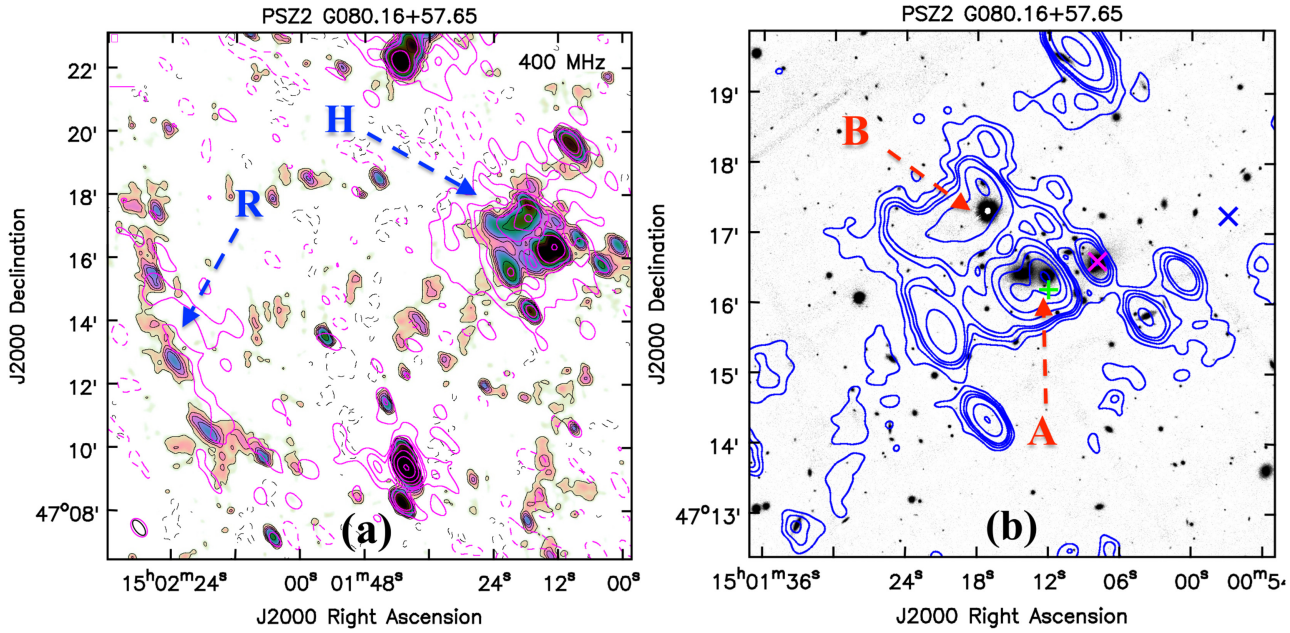

Figure 4. (a) uGMRT high-resolution colour map and contours (black) and LoTSS-I contours (magenta) for the cluster PSZ2 G080.16+57.65 (contours are at the same level as Fig. 1a with rms noise $\sigma = 55$ and 240 μJy beam^{-1}, respectively). (b) uGMRT contours (blue) plotted over the Pan-STARRSI *i*-band image, zoomed in to the central halo region. The centre of the GMBCG J225.28318+47.27663 cluster, clearly associated with this source, is shown as a magenta cross. The physical scale for the images is 1.64 kpc arcsec^{-1}.

but at an unusual distance of 1.3 Mpc away from the cluster centre, beyond the virial radius (self-similar fiducial $r_{200} \sim 1.2$ Mpc). The spectral index of $\alpha_{144}^{400} \sim -1.4$, as computed using our uGMRT and 144-MHz fluxes (reported in van Weeren et al. 2020), as well as its peripheral location and bow-like shape, suggest that it is a steep-spectrum radio relic.

The only radio point source found inside this cluster (in the NED) is a radio galaxy, exactly at the centre of the Abell cluster (green '+' in Fig. 4b), and at a similar redshift $z = 0.0873$, confirming it to be a member of the cluster. This also matches with a radio peak seen in our uGMRT map (see 'A' in Fig. 4b). The other bright but extended radio source ('B') in the uGMRT and LoTSS-I maps cannot be seen in the VLA Faint Images of the Radio Sky at Twenty-cm (FIRST) survey or any other higher-frequency radio surveys. There is no optical source in the NED identified as a galaxy that coincides with B, which confirms its nature as a diffuse radio source.

We produced a point-source subtracted image to map the central diffuse emission in this cluster, following the method described in Section 2. We found a halo-like emission with a size ∼540 × 490 kpc and flux density $S_{400} = 19.3 \pm 2.0$ mJy (see Fig. 5) within 3σ contours. Unlike van Weeren et al. (2020), we found no radio bridge connecting the relic and the halo, in our uGMRT point-source removed maps, which have an rms of $\sigma = 120$ μJy beam^{-1}.

Fig. 5 reveals an elongated and clumpy X-ray map, indicative of a non-relaxed state. The radio structure uncovered here is found to be well enclosed by the bigger X-ray clump, the peak of which also coincides with the centre of cluster GMBCG J225 (magenta '×'), establishing its connection to the ICM of the cluster. Following an alternative method of estimating the flux density of the radio-halo, as described in Section 2, we computed a flux density of 18.0 ± 0.01 mJy within three times the e-folding radius (see Table 3). In comparison, van Weeren et al. (2020) computed a flux density of 92 mJy for the same halo, giving rise to an average spectral index $\alpha_{144}^{400} \sim -1.6$. Though this is indicative of an ultra-steep spectrum radio halo, the

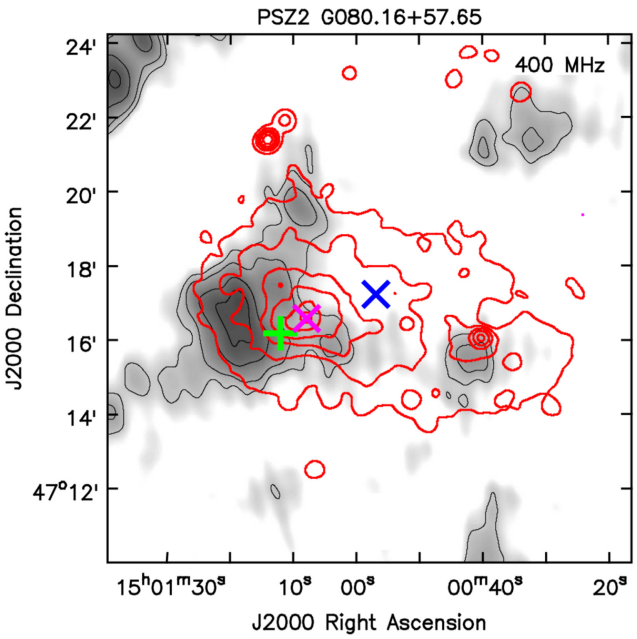

Figure 5. *XMM* contours (red) over the uGMRT point-source subtracted map of the source PSZ2 G080.16+57.65.

radio emission is neither centrally located as in archetypal radio haloes, nor found at the cluster outskirts as are the radio relics, making it difficult to firmly assign an identity to it.

3.4 PSZ2 G106.61+66.71, an intermediate halo?

PSZ2 G106.61+66.71 is the highest redshift ($z = 0.33140$) cluster in our sample detected with diffuse radio emission. This is a rich

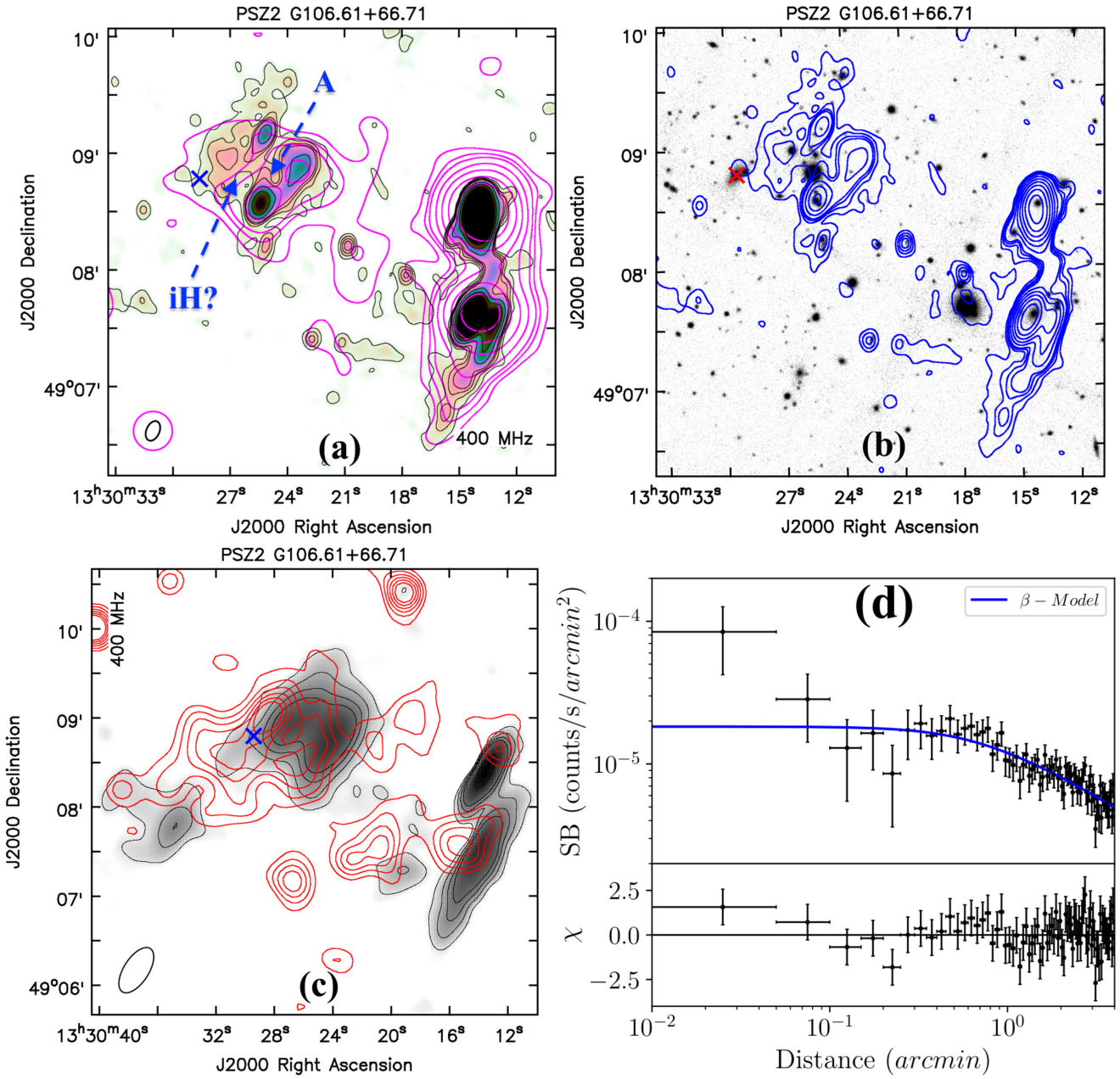

Figure 6. (a) uGMRT high-resolution colour map and contours (black) and LoTSS-I contours (magenta) for the cluster PSZ2 G106.61+66.71 (contours are at the same level as Fig. 1a with rms noise $\sigma = 45$ and 300 μJy beam^{-1}, respectively). (b) uGMRT contours (blue) over Pan-STARRSI *i*-band image. (c) *Chandra* contours (red) over uGMRT point-source subtracted map. Radio contours are at 3, 5, 7, 9, 18, 36 $\times$ σ with $\sigma = 120$ μJy beam^{-1}. (d) X-ray surface brightness profile fitted with β-model and the residuals for the circular annuli centred at the X-ray peak. The physical scale for the images is 4.76 kpc arcsec^{-1}

cluster with 82 galaxy members within a radius $r_{200} = 1.76$ Mpc (Wen & Han 2013) with an SZ mass $M_{500}^{\rm SZ} = 4.67^{+0.55}_{-0.57} \times 10^{14}\,{\rm M}_{\odot}$ (Planck-16). The BCG in this cluster is a radio bright source (NVSS J133024+490846, 'A') and about 180 kpc away from the *Chandra* X-ray peak (see Fig. 6a and c).

Both the uGMRT and LoTSS-I ($\sigma_{144} = 300$ μJy beam^{-1}) radio maps show an indication of an extended diffuse emission around the BCG (see Fig. 6a). To study the diffuse emission in detail, we produced a point-source subtracted uGMRT image using the method described in Section 2. The contours of this image (black; Fig. 6c) reveal that the diffuse emission has an extent of at least $\sim$550 $\times$ 530 kpc. The computed flux density (using the profile fit method described in Section 2) is 6.6 $\pm$ 0.01 mJy within three times the e-folding radius (i.e. $3r_{\rm e} = 507 \pm 17$; see Table 3) for our uGMRT map. At 144 MHz, using the same method, the flux is estimated to be 20 mJy (van Weeren et al. 2020). This leads to an average spectral index of $\alpha_{144}^{400} \sim -1.09$.

The value of the radio power estimated from these values is rather high, $P_{1.4\,{\rm GHz}} = 6.34 \pm 0.19 \times 10^{23}$ W Hz^{-1} at 1.4 GHz. Such an emission feature is usually seen in cool-core clusters as radio mini-haloes, albeit usually with an extent less than 500 kpc. Our *Chandra* X-ray analysis shows a low-brightness core with non-smooth profile (see Fig. 6d), usually a feature of a weak cool-core cluster. X-ray maps also show elongation and substructures (red

Table 4. Parameters for $P_{1.4\,\mathrm{GHz}}$–M_{500} and $P_{1.4\,\mathrm{GHz}}$–LLS correlations.

Object name (structure)	Spectral index	$P_{1.4\,\mathrm{GHz}}$ (10^{23} W Hz^{-1})	Relic LLS (kpc)
PSZ2 G080 (H)	−1.60	0.49 ± 0.01	–
(R)	−1.40	0.46 ± 0.01	1000
PSZ2 G089 (R)	−1.08	0.20 ± 0.05	205
PSZ2 G106 (H)	−1.08	6.34 ± 0.19	–
PSZ2 G111 (R)	−1.40	8.68 ± 1.26	750

contours in Fig. 6c). The total X-ray luminosity of the cluster is on the high side $L_X = 3.97^{+0.4}_{-0.3} \times 10^{44}$ erg s^{-1}, given its velocity dispersion, indicative of a merger.

This is not the typical scenario for a mini-halo found in relaxed, cool-core clusters. Thus, a second possibility is that the cool core in this cluster has been dislodged from its original location due to a recent merger. Therefore, the radio emission in PSZ2 G106 may be an intermediate radio halo, similar to other cases reported by, for instance, Savini et al. (2018), Kale, Shende & Parekh (2019) and Raja et al. (2020).

3.5 Correlations between radio power of haloes and relics and other parameters

Following the early work by Venturi et al. (2008), which helped to establish the link between the existence of radio haloes and the recent merger history of clusters, the correlation of halo power (commonly estimated at 1.4 GHz; e.g. Cassano et al. 2010) with various cluster parameters, gives an insight into the origin and nature of these haloes, and helps us further establish the physical processes responsible for these systems.

In this context, the widely used correlation for cluster mass (M_{500}) and radio halo power at 1.4 GHz ($P_{1.4}$) has been computed by Cassano et al. (2013) using a sample of predominantly massive clusters ($>5 \times 10^{14}$ M$_\odot$). A correlation has also been reported for the relic power (at 1.4 GHz) and its size (LLS) by Feretti et al. (2012), and recently updated by Paul et al. (2020). However, as discussed and reported in this study, in the age of uGMRT and LoFAR, as the number of detections dramatically increase, one needs to validate the scaling relations, especially as detections are pushed to lower cluster masses.

In this work, in total, we detect two possible radio haloes and three radio relics. In order to include them in this correlation study, the observed radio power with uGMRT at 400 MHz is scaled to that at 1.4 GHz, assuming the spectral indices reported in this paper (see Table 4). SZ masses (M^{SZ}_{500}) are used for all the clusters for which they are available.

Fig. 7(a), the correlation plot of radio halo power ($P_{1.4\,\mathrm{GHz}}$) versus the cluster mass (M_{500}), shows the data from Cassano et al. (2013), updates from van Weeren et al. (2019) and two objects reported in this paper. While the Cassano et al. (2013) sample yields a BCES bisector slope $\alpha_{\mathrm{BCES}} = 3.70 \pm 0.63$, the combined correlation slope with all the above-mentioned data is found to be $\alpha_{\mathrm{comb}} = 3.40 \pm 0.32$, slightly flatter, though having well-overlapping error limits.

The data for the radio relic power ($P_{1.4\mathrm{GHz}}$) versus the relic size (*LLS*) correlation plot shown in Fig. 7(b) are largely updated from van Weeren et al. (2019) and Paul et al. (2019), along with three objects from this study. A new slope $\alpha_{\mathrm{new}} = 2.48 \pm 0.19$ is found to be fairly consistent with the correlation of $\alpha = 2.39 \pm 0.19$ computed from the data found in the literature. We note that the relic of PSZ2G 080 is a far outlier, having a very low radio emission power considering its large LLS. Interestingly, this is so far the only relic found beyond the virial radius ($>r_{200}$) of the host cluster.

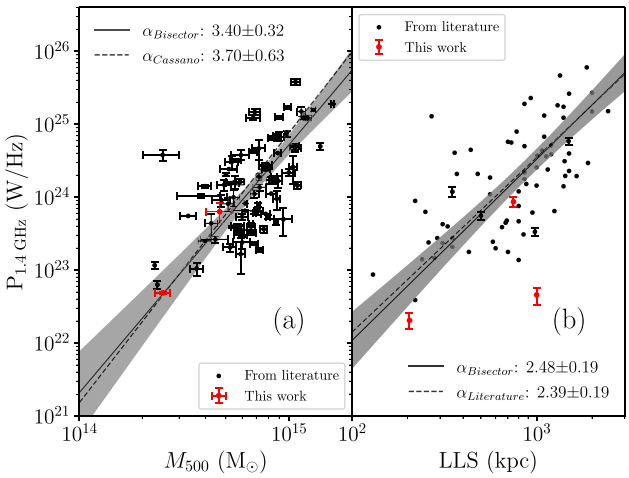

Figure 7. (a) The radio power at 1.4 GHz of radio haloes versus the mass of the host cluster within R_{500} (M_{500}). (b) The radio power at 1.4 GHz of radio relics ($P_{1.4\,\mathrm{GHz}}$) versus the largest linear size (LLS) of the relics. The objects studied in this paper are marked in red. The samples are discussed in Section 3.5.

4 SUMMARY AND CONCLUSIONS

We present the results from the first systematic search for diffuse radio emission from low-mass clusters ($<5 \times 10^{14}$ M$_\odot$), in the overlap region of the *Planck* SZ catalogue (PSZ2) and the LoTSS-1, confirmed by deep uGMRT maps at 400 MHz obtained by us. Out of 12 clusters in our sample (see Section 2), four are detected with diffuse radio emission. The peripheral structures detected in the PSZ2 G111 and PSZ2 G080 clusters are the steep-spectrum relics. In the absence of accurate spectral properties, similar emission found in PSZ2 G089 is currently speculated to be that from a relic. Cluster PSZ2 G080 also hosts a radio halo along with the relic, and PSZ2 G106 is detected only with a central diffuse emission, argued to be an intermediate radio halo.

In this context, it is important to mention that the cluster PSZ2 G089, with $M^{SZ}_{500} = 1.8 \times 10^{14}$ M$_\odot$, is among the lowest-mass clusters detected with a radio relic, and PSZ2 G080 with $M^{SZ}_{500} = 2.5 \times 10^{14}$ M$_\odot$ is the lowest-mass cluster to host both a radio halo and an Mpc-size relic. In the latter case, the relic, at a distance 1.3 Mpc from the cluster centre, is the only such specimen in a cluster with the relic found beyond the virial radius, and it is an outlier in the scaling relation between radio relic power and spatial extent. With these new detections, we update the $P_{1.4\,\mathrm{GHz}}$–M_{500} correlation in a much wider range of masses, especially towards the lower-mass end.

We note that the unavailability of corrected LoTSS-I images (i.e. LoTSS-II images) in the public domain restricted us from making the spectral index maps that would provide further indications for the accurate classification of these sources. Nevertheless, the results obtained from our sample consisting of a small number of low-mass clusters are crucial, considering their rarity, and the implications of their existence on the study of non-thermal emission mechanisms over a wide range of masses of such systems. This also motivates us to examine low-mass clusters with Square Kilometre Array (SKA) precursors, such as uGMRT and MeerKAT, etc., using a larger data set.

ACKNOWLEDGEMENTS

This research was funded by DST INSPIRE Faculty Scheme awarded to SP (code: IF-12/PH-44). PG acknowledges the Council of Scientific & Industrial Research (CSIR) for a Senior research fellowship (CSIR-SRF; file no: 09/137(0574)/2018 EMR-1). S. Salunkhe wants to thank 'Bhartratna JRD Tata Gunwant Sanshodhak Shishyavruti Yojna' for a doctoral fellowship. S. Sonkamble acknowledges a financial contribution from ASI-INAF n.2017-14-H.0 (PI: A. Moretti). We thank the Director, NCRA-TIFR, for granting discretionary time on uGMRT, and the staff of the GMRT for making these observations possible. GMRT is run by the National Centre for Radio Astrophysics of the Tata Institute of Fundamental Research.

DATA AVAILABILITY

The uGMRT data can be accessed from the GMRT data archive at https://naps.ncra.tifr.res.in/goa/data/search. The calibrated data can be shared on reasonable request to the corresponding author. The LoTSS-I data can be sourced from the public domain archive at https://lofar-surveys.org/surveys.html.

REFERENCES

Bernardi G. et al., 2016, MNRAS, 456, 1259
Botteon A., et al., 2019, A&A, 630, A77
Cassano R., Brunetti G., Röttgering H. J. A., Brüggen M., 2010, A&A, 509, A68
Cassano R. et al., 2013, ApJ, 777, 141
Cuciti V. et al., 2021, A&A, 647, A51
de Gasperin F. et al., 2017, A&A, 597, A15
Dwarakanath K. S., Parekh V., Kale R., George L. T., 2018, MNRAS, 477, 957
Eckert D., Molendi S., Paltani S., 2011, A&A, 526, A79
Feretti L., Giovannini G., Govoni F., Murgia M., 2012, A&AR, 20, 54
Ferrari C., Govoni F., Schindler S., Bykov A. M., Rephaeli Y., 2008, Space Sci. Rev., 134, 93
Flin P., Krywult J., 2006, A&A, 450, 9
Gaspari M., Brighenti F., D'Ercole A., Melioli C., 2011, MNRAS, 415, 1549
Giacintucci S., Markevitch M., Cassano R., Venturi T., Clarke T. E., Kale R., Cuciti V., 2019, ApJ, 880, 70
Gupta Y. et al., 2017, Current Sci., 113, 707
Hao J. et al., 2010, ApJS, 191, 254
Hoang D. N. et al., 2019, A&A, 622, A21
Ignesti A., Brunetti G., Gitti M., Giacintucci S., 2020, A&A, 640, A37
Intema H. T., Jagannathan P., Mooley K. P., Frail D. A., 2017, A&A, 598, A78
John R. S., Paul S., Iapichino L., Mannheim K., Kumar H., 2019, MNRAS, 488, 1301
Kale R., Wik D. R., Giacintucci S., Venturi T., Brunetti G., Cassano R., Dallacasa D.,de Gasperin F.,2017, MNRAS, 472, 940
Kale R., Shende K. M., Parekh V., 2019, MNRAS, 486, L80
Knowles K. et al., 2019, MNRAS, 486, 1332
Lovisari L., Reiprich T. H., Schellenberger G., 2015, A&A, 573, A118
McMullin J. P., Waters B., Schiebel D., Young W., Golap K., 2007, inShaw R. A.,Hill F.,Bell D. J., eds,ASP Conf. Ser. Vol. 376, Astronomical Data Analysis Software and Systems XVI.Astron. Soc. Pac.,San Francisco, p.127
Murgia M., Govoni F., Markevitch M., Feretti L., Giovannini G., Taylor G. B., Carretti E., 2009, A&A, 499, 679
Nikiel-Wroczyński B. et al., 2019, A&A, 622, A23
Offringa A. R., McKinley B., Hurley-Walker N., Briggs F. H., Wayth R. B., Kaplan D. L., Bell M. E. et al., 2014, MNRAS, 444, 606
Paul S., John R. S., Gupta P., Kumar H., 2017, MNRAS, 471, 2
Paul S., Salunkhe S., Datta A., Intema H. T., 2019, MNRAS, 489, 446
Paul S., Salunkhe S., Sonkamble S., Gupta P., Mroczkowski T., Raychaudhury S., 2020, A&A, 633, A59
Planck Collaboration XXVII, 2016, A&A, 594, A27 (Planck-16)
Raja R. et al., 2020, MNRAS, 493, L28
Sarazin C. L., 2002, inFeretti L.,Gioia I. M.,Giovannini G. (eds),ASSL Vol. 272, Merging Processes in Galaxy Clusters.Kluwer,Dordrecht, p.1
Savini F. et al., 2018, MNRAS, 478, 2234
Shimwell T. W. et al., 2019, A&A, 622, A1
Struble M. F., Rood H. J., 1999, ApJS, 125, 35
van Weeren R. J., de Gasperin F., Akamatsu H., Brüggen M., Feretti L., Kang H., Stroe A.,Zandanel F. 2019, Space Sci. Rev., 215, 16
van Weeren R. J. et al., 2020, preprint (arXiv:2011.02387)
Venturi T., Giacintucci S., Dallacasa D., Cassano R., Brunetti G., Bardelli S., Setti G., 2008, A&A, 484, 327
Wen Z. L., Han J. L., 2013, MNRAS, 436, 275

This paper has been typeset from a TEX/LATEX file prepared by the author.